CHEMISTRY OF MATERIALS

pubs.acs.org/cm

Article

Electron-Enhanced Deposition of Titanium-, Silicon- and Tungsten-Containing Films at Low Temperatures Using Volatile Precursors with Various Reactive Background Gases

Zachary C. Sobell, Andrew S. Cavanagh, and Steven M. George*

Cite This: *Chem. Mater.* 2025, 37, 4652−4664

Read Online

ACCESS | Metrics & More | Article Recommendations | Supporting Information

ABSTRACT: Electron-enhanced atomic layer deposition (EE-ALD) and electron-enhanced chemical vapor deposition (EE-CVD) can be employed for the low temperature deposition of thin films using volatile precursors with various reactive background gases (RBGs). EE-CVD expands on the previous demonstration of TiN EE-ALD using alternating $Ti(N(CH_3)_2)_4$ (tetrakisdimethylamino titanium (TDMAT)) and electron beam exposures with NH_3 RBG. During EE-CVD, the electron beam and the RBG are present continuously. Together with the RBG and electron beam incident on the surface, the volatile precursor is pulsed into the vacuum chamber to control the film growth. In this survey, the metal or metalloid precursors were TDMAT, Si_2H_6, and $W(CO)_6$. The RBGs were O_2, NH_3, CH_4, and H_2. The study focused on TiO_2 EE-ALD and SiN, SiO_2, SiC_x, SiH_x, W_2N, WO_x, and WC_x EE-CVD. Thin film growth was monitored using in situ 4-wavelength ellipsometry. To first illustrate EE-ALD, TiO_2 EE-ALD was performed at $T < 80$ °C using alternating TDMAT and electron beam exposures together with O_2 RBG. The growth rate for the TiO_2 EE-ALD was ∼0.7 Å/cycle. The TiO_2 EE-ALD films were nearly stoichiometric, displayed crystallinity, and were smooth as measured by atomic force microscopy (AFM). Other Ti-containing EE-ALD films were deposited using CH_4 and H_2 RBGs. Subsequently, to demonstrate EE-CVD, SiC_x EE-CVD was performed at $T <$ 100 °C using repeating Si_2H_6 pulses with continuous electron beam and CH_4 RBG exposures. XPS revealed a 1:1 Si/C stoichiometry for a CH_4 RBG pressure of 0.45 mTorr and C-rich films for higher CH_4 RBG pressures. The SiC EE-CVD growth rate was ∼0.4 Å per Si_2H_6 pulse. The stoichiometric SiC EE-CVD films were smooth as measured by AFM. Other Si-containing EE-CVD films that were deposited included SiO_2, SiN and SiH_x. In addition, W_2N was deposited with EE-CVD at $T < 120$ °C using repeating $W(CO)_6$ pulses with continuous electron beam and NH_3 RBG exposures. The W_2N EE-CVD growth rate was ∼0.17 Å per $W(CO)_6$ pulse. The W_2N films had a resistivity of ∼450 $\mu\Omega$ cm. The W_2N EE-CVD films also displayed crystallinity and high purity. Other W-containing EE-CVD films that were deposited included WO_x and WC_x. This survey shows that the EE-ALD technique can be extended to EE-CVD with various RBGs to deposit a broad range of materials at low temperatures including oxides, nitrides and carbides.

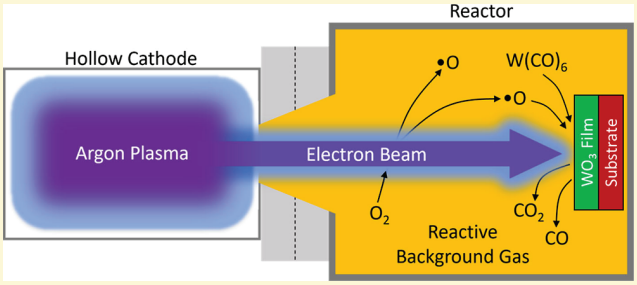

1. INTRODUCTION

Low energy electrons can deposit films of semiconductors, metals, and dielectrics by electron-enhanced atomic layer deposition (EE-ALD) at low temperatures. EE-ALD has been previously used to deposit GaN, Si, BN, Co, Ru, and SiO_2 films in a high vacuum environment.[1−7] EE-ALD employs alternating exposures of precursors and low energy electrons at ≤100−150 eV to deposit thin films as shown in Figure 1a. EE-ALD is a nonthermal process and can deposit materials at temperatures <100 °C. During EE-ALD, the precursor adsorbs on the substrate. Subsequent electron exposure leads to a loss of ligands from the adsorbed precursor through electron stimulated desorption (ESD).[8] The desorbed ligands leave behind open sites that are then available for further precursor adsorption. Repeating the alternating precursor doses and electron exposures yields EE-ALD growth.

The deposition of Si from disilane (Si_2H_6) can be considered a model system for EE-ALD.[4] Silicon was deposited at room temperature using sequential surface reactions with Si_2H_6 and low energy electrons as the reactants.[4] In comparison, silicon growth by thermal ALD requires temperatures of 775−890 °C using $SiH_2Cl_2 + H_2$,[9] or temperatures of 540−650 °C using SiH_2Cl_2 + H atoms.[10] The proposed mechanism for Si EE-ALD was dissociative adsorption of Si_2H_6 on the surface and then the removal of hydrogen by ESD using

Received: February 2, 2025
Revised: May 30, 2025
Accepted: June 2, 2025
Published: June 16, 2025

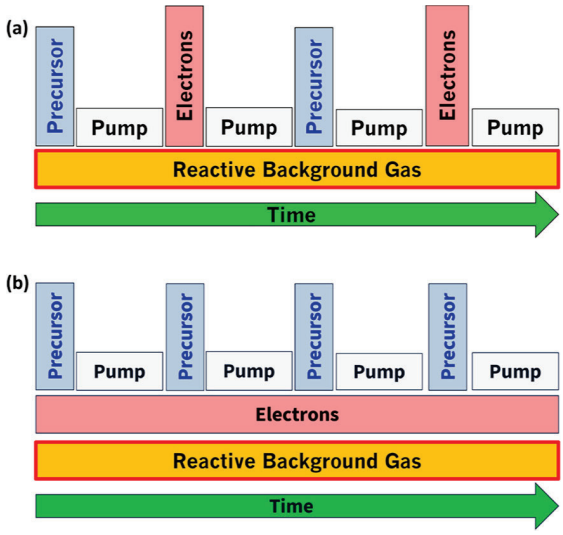

Figure 1. (a) EE-ALD process using alternating precursor and electron exposures with continuous reactive background gas (RBG) exposure. (b) EE-CVD process using repeating precursor doses with continuous electron and reactive background gas (RBG) exposures.

low energy electrons. The removal of hydrogen from the surface leaves behind dangling bonds on the silicon surface. These dangling bonds are then available for subsequent Si_2H_6 adsorption. Silicon growth rates were determined to be 0.3 Å/cycle at room temperature and an electron energy of 100 eV.[4] Calculations showed that this growth rate agreed well with the predicted growth rate based on the dissociative adsorption of Si_2H_6 on the dangling bonds of a Si surface.[4]

There are some similarities between EE-ALD and focused electron beam induced deposition (FEBID) techniques.[11] EE-ALD uses sequential exposures of precursors and electrons to deposit thin films with atomic layer control over large surface areas >10 cm^2.[1] In contrast, FEBID uses a continuous focused electron beam in the presence of a precursor to produce the deposition.[11] The main goal of FEBID is to form nanostructure features using a direct-write approach.[11] The deposition thickness during FEBID is controlled by the processing time. The energies employed for EE-ALD and FEBID are also very different. EE-ALD uses low energy electrons in the range of 100−150 eV where the inelastic electron mean free path is at a minimum at ∼5−7 Å and the electrons interact primarily with the surface. FEBID uses electrons at higher energies around 1−50 keV where the electron beams can be focused to minimum spot sizes.[11] However, the actual chemistry induced by FEBID is thought to occur by secondary electrons at much lower electron energies.[12]

Both EE-ALD and FEBID can have problems with the purity of the deposition. The impurities during FEBID result from the fragmentation of the FEBID precursors during electron bombardment.[13−16] Postdeposition cleaning with electron beams and reactive gases after FEBID is one method to improve purity.[17−19] Some studies have also introduced background gases during FEBID to obtain higher purity films.[20−22] The introduction of a reactive background gas (RBG) during EE-ALD was also recently shown to enhance film purity and favorably modify film composition during EE-ALD.[23]

The presence of both the RBG and electron beam during EE-ALD is possible because of the chemical insensitivity and large operating pressure range of the hollow cathode plasma electron source (HC-PES).[1] During TiN EE-ALD, alternating TDMAT and low energy electrons deposited an impure TiC_xN_y film.[23] In contrast, the introduction of an NH_3 RBG during the entire TiN EE-ALD cycle led to the deposition of highly pure, low resistivity, crystalline TiN film.[23] The interaction of NH_3 and low energy electrons was believed to create reactive $\bullet NH_2$ and $\bullet H$ radicals that removed C and O impurities by creating volatile CH_4, CH_3NH_2, NO_x, or H_2O products.

The current work continues the focus on introducing the RBG together with the electron exposures to deposit thin films.[23] The metal or metalloid precursor is also pulsed during the continuous electron and RBG exposures. This procedure defines electron-enhanced chemical vapor deposition (EE-CVD) with a RBG illustrated in Figure 1b. EE-CVD shifts the role of the low energy electrons from an intermittently dosed reactant in EE-ALD to the role of a continuously dosed reactant in EE-CVD. EE-CVD is not a self-limiting process. However, deposition times can be much faster for EE-CVD than for EE-ALD. There also may be synergies that lead to improved properties of the EE-CVD films.

This paper explores EE-ALD and EE-CVD with RBGs. Titanium-, silicon- and tungsten-containing films are deposited using TDMAT, Si_2H_6, and $W(CO)_6$ precursors, respectively. These films are grown as oxides, nitrides and carbides using O_2, NH_3 and CH_4 RBGs, respectively. Silicon films are also deposited using Si_2H_6 with a H_2 RBG. The results illustrate the broad range of materials that can be grown by EE-ALD and EE-CVD at low temperatures using simple metal or metalloid precursors together with various RBGs.

2. EXPERIMENTAL SECTION

2.1. Vacuum Chamber and Accessories. The EE-ALD and EE-CVD films were grown in a vacuum apparatus that has been described previously.[1−5,23] The main vacuum chamber was pumped by a turbomolecular pump. This turbomolecular pump has a pumping speed of 245 L/s for Ar (HiPace 300 P, Pfeiffer Vacuum Technology AG). This turbomolecular pump was also backed by a smaller turbomolecular pump operating at a pumping speed of 67 L/s for Ar (HiPace 80, Pfeiffer Vacuum Technology AG). This smaller turbomolecular pump was backed by a rotary vane pump (Pascal 2010 SD 10 m^3/h, Pfeiffer Vacuum Technology AG). Additionally, the main vacuum chamber can be pumped by an ion pump (TiTan 100L Variable Element, 100 L/s, Gamma Vacuum). A valve can separate this ion pump from the main chamber. The main vacuum chamber had a base pressure of 2×10^{-9} Torr using both the ion and turbomolecular pumps.

The chamber was equipped with a load lock that allowed samples to be introduced without breaking vacuum. The main chamber also contained a 4-wavelength in situ ellipsometer (Filmsense1) and mass spectrometer (PrismaPlus QMG 220, Pfeiffer Vacuum). The chamber was also equipped with a cold cathode gauge (MKS) to measure pressure. In addition, a picoammeter (Keithley) was attached to the sample stage to measure the electron current incident on the sample and sample stage from the electron source. Sample temperature was measured with a thermocouple held in contact with the coupon surface with a clip. An analysis chamber containing an in vacuo Auger electron spectroscopy (AES) spectrometer (RBD, microCMA) was also attached to the main chamber.

2.2. Hollow Cathode Plasma Electron Source. The electron source was a hollow cathode plasma electron source (HC-PES) that has been described in detail earlier.[1] Figure 2a shows a schematic of the HC-PES.[1] The argon (Airgas, 99.999%) plasma was sparked in the hollow cathode body. Low energy electrons were extracted with a bias grid. The electrons exited the HC through an aperture. Argon gas

https://doi.org/10.1021/acs.chemmater.5c00264
Chem. Mater. 2025, 37, 4652−4664

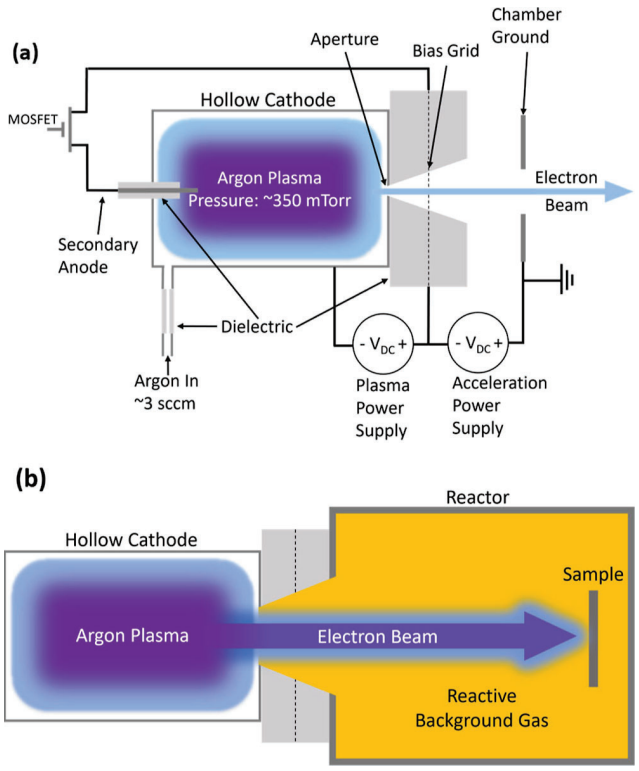

Figure 2. (a) Schematic of hollow cathode plasma electron source (HC-PES) showing electrical diagram, gas flow, approximate pressures, plasma in hollow cathode cavity, and emitted electron beam. (b) Schematic of HC-PES interfacing with reactor, depicting electron beam traveling though the reactive background gas (RBG) and impinging on the sample.

also leaked through this aperture and produced a pressure of ~1 mTorr in the reactor. All the work in this study used an applied voltage of 100 V to the bias grid. This applied voltage accelerated the electrons leaving the aperture.

Figure 2b displays a schematic of the HC-PES and the electron beam accelerated to the sample. The electrons were separated from any sputtered material from the hollow cathode plasma using electron optics.[1] The electrons also traveled through the argon gas and the RBG on their path to the sample. The distance between the bias grid located close to the aperture and the sample was approximately 30 cm.[1] The electrons were incident on the sample at normal incidence. The electron currents were in the range of 30−80 mA. The electron energy defined by the grid bias was ≤100 eV. Electrons at ~100 eV interact strongly with the surface and are known to have high electron stimulated desorption cross sections.[24] The electron beam irradiated an area of ~10 cm^2. The samples started each experiment at room temperature at 21 °C. The interaction between the low energy electrons and the substrate led to sample heating. However, the sample temperature never exceeded 120 °C.

2.3. Reactive Background Gases and Substrates. The reactive background gas (RBG) (NH_3 Matheson, 99.9992%, O_2 Airgas, 99.995%, H_2 Matheson, 99.9992%, or CH_4 Matheson, 99.9995%) flowed into the chamber though a leak valve and was present continuously during the EE-ALD or EE-CVD deposition processes. The RBG pressure was ~1 mTorr for H_2, NH_3, and O_2 as measured by the cold cathode pressure gauge (MKS) under constant pumping using the turbomolecular pump. The CH_4 RBG pressure was varied between 3×10^{-5} Torr and 1 mTorr depending on the experiment.

The background gases in the chamber will cause some electron scattering. The RBG pressure typically varied from the high 10^{-4} Torr range to the mid 10^{-3} Torr range. This pressure range allows for electron beam interaction with the RBG without excessive electron scattering. This pressure window leads to the creation of gas-phase radicals that can influence the film composition. In addition, the electron beam is also incident on the substrate at normal incidence for electron−surface interactions such as electron stimulated desorption.

The EE-ALD and EE-CVD were conducted on Si wafer coupons (Silicon Valley Microelectronics, boron-doped). There was a native oxide on the silicon surface for all films. The only exception was SiH_x EE-CVD where the SiH_x films were grown from Si_2H_6 with a H_2 RBG. SiH_x was deposited on a 1 μm TiN film on a Si wafer to distinguish the SiH_x EE-CVD from the Si substrate. Prior to insertion into the vacuum apparatus, all the Si native oxide coupons were sonicated in dilute Alconox Detergent, rinsed in DI water, then blown dry with ultrahigh purity nitrogen. The TiN coupon was cleaned with methanol and acetone, then blown dry with UHP N_2. The coupons were then loaded into the load lock chamber following procedures that have been detailed earlier.[1]

2.4. EE-ALD and EE-CVD Pulse Sequences. TiO_2 EE-ALD was conducted according to Figure 1a using alternating precursor and electron beam exposures. The pulse sequence was: (1) TDMAT exposure; (2) pumping before electron beam exposure; (3) electron beam exposure; and (4) pumping before the next TDMAT exposure. The timing for this pulsing sequence can be characterized by (t_1, t_2, t_3, t_4). The TDMAT precursor was maintained at 0.3 Torr behind a micropulse valve. The TDMAT bubbler was heated to ~45 °C to achieve the required vapor pressure. The valve was actuated for t_1 = 1 s. The valve opening led to a transient pressure in the main chamber of 4×10^{-7} Torr as measured by the cold cathode gauge in an empty reactor. Pumping was then continued for t_2 = 1 s after the TDMAT exposure.

Subsequently, the electron exposure was performed with a grid bias of 100 V for t_3 = 5 s, with an electron current measured at the sample stage of ~65 mA. The next TDMAT exposure was then conducted after continued pumping for t_4 = 1 s after the electron exposure. The timing for this pulsing sequence was (1, 1, 5, 1). The sum of these steps produced a reaction cycle time of ~8 s. Note that the turbomolecular pump was pumping on the main vacuum chamber during the entire pulse sequence.

SiC_x EE-CVD was conducted according to Figure 1b using repeating Si_2H_6 exposures. In addition, the electron beam and the CH_4 RBG were continuously present during the repeating Si_2H_6 exposures. The CH_4 RBG pressure was 0.45−1 mTorr. The pulse sequence was: (1) Si_2H_6 exposure; and (2) pumping time before next Si_2H_6 exposure. The timing for this pulsing sequence can be characterized by (t_1, t_2). The Si_2H_6 precursor was maintained at 1 Torr behind a micropulse valve. The valve was actuated for t_1 = 0.1 s. The valve opening led to a transient pressure in the main chamber of 4×10^{-6} Torr as measured by the cold cathode gauge in an empty reactor.

Pumping was then continued for t_2 = 1.3 s. This pumping time allowed the precursor time to regenerate the 1 Torr pressure behind the micropulse valve before the next precursor dose. The sum of these steps produced a cycle time of ~1.4 s. The electron beam remained on during the entire deposition sequence. The bias grid of the HC-PES was set at 100 V with a current measured at the sample stage of ~50 mA. Note that the turbomolecular pump was also pumping on the main vacuum chamber during the entire deposition sequence.

W_2N EE-CVD was performed according to Figure 1b using repeating $W(CO)_6$ exposures. The electron beam and the NH_3 RBG were continuously present during the repeating $W(CO)_6$ exposures. The NH_3 RBG pressure was 2 mTorr. The pulse sequence was: (1) $W(CO)_6$ exposure; and (2) pumping time before the next $W(CO)_6$ exposure. The timing for this pulsing sequence can be characterized by (t_1, t_2). The $W(CO)_6$ precursor was maintained at 0.3 Torr behind a micropulse valve. The $W(CO)_6$ bubbler was heated to ~100 °C to achieve the required vapor pressure. The valve was actuated for t_1 = 1 s. The valve opening led to a transient pressure in the main chamber of 1×10^{-5} Torr as measured by the cold cathode gauge in an empty reactor.

Pumping was then continued for t_2 = 5 s. This pumping time allowed the precursor time to regenerate the 0.3 Torr pressure behind the micropulse valve before the next precursor dose. The sum of these

https://doi.org/10.1021/acs.chemmater.5c00264
Chem. Mater. 2025, 37, 4652−4664

steps produced a cycle time of ~6 s. The electron beam was kept on during the entire deposition sequence. The bias grid was set at 100 V with a current measured at the sample stage of ~73 mA. The turbomolecular pump was pumping on the main vacuum chamber during the entire deposition sequence.

Unless otherwise noted, the reaction conditions described for TiO_2, SiC, and W_2N are generic for the other films grown from TDMAT, Si_2H_6, and $W(CO)_6$ with the various RBGs. The precursor pressures at the sample was higher for TDMAT, $W(CO)_6$, and Si_2H_6 than the reported pressure transients because the micropulse valve used to dose the precursors was connected to a 1″ diameter tube that led to the sample and ended ~5 cm from the sample. The cold cathode measured the precursor pressure transient after the pressure transient had diffused into the entire chamber and been pumped by the turbomolecular pump.

2.5. Ellipsometry, X-ray Reflectivity, and X-ray Photoelectron Spectroscopy. In situ 4-wavelength ellipsometry measurements were collected every second throughout the deposition. The in situ ellipsometer (Filmsense FS-1) used four wavelengths of light. The precision of the in situ 4-wavelength ellipsometry measurements of film thickness was within ±0.03 Å. Most films were modeled with a Tauc-Lorentz model. SiO_2 was modeled with a Cauchy model. Nitrides and carbides of Ti and W were modeled with a Drude-Lorentz model to obtain the film resistivities. The longest wavelength employed in the FS-1 ellipsometer is 660 nm. This wavelength is not sufficient for fully modeling the Drude term, and as such the resistivities are estimations.

Ex situ spectroscopic ellipsometry (Model M-2000, J.A. Woollam Co., Inc.) was also performed to measure the film thickness of some samples after removing them from the reactor. Ex spectroscopic ellipsometry was used to corroborate the in situ resistivity measurements. AFM measurements were used to monitor film roughness. The ex situ AFM measurements were performed with an AFM instrument (Park NX10) using noncontact mode. The scan rate was 0.3−0.8 Hz for a 1 × 1 μm area using a micro cantilever probe (Olympus, OMCL-AC160TS).

X-ray reflectivity (XRR) was used to determine film thickness and density. Grazing incidence X-ray diffraction (GI-XRD) determined crystallinity of the films. Both GI-XRD and XRR scans were performed using a XRD instrument (Bede D1, Jordan Valley Semiconductors) with radiation from Cu Kα (λ = 1.540 Å). The X-ray tube filament voltage was 40 kV and the current was 35 mA. The incident angle used for GI-XRD was 0.3°. The XRR scan range was 300 to 6000 arcsec with a 5 arcsec step size. The XRR scans were analyzed using modeling software (REFS, Jordan Valley Semiconductors). XRR analysis could not be used to measure the film thickness of all the EE-CVD films. Since the film thickness is dependent on electron flux during EE-CVD, some EE-CVD films had insufficient uniformity to produce fringes that could be accurately modeled by XRR.

The film composition was determined using an X-ray photoelectron spectrometer (XPS) (PHI 5600) using a monochromatic Al Kα source with an energy of 1486.6 eV. The pass energy was 58.7 eV, the step size was 0.25 eV, and the dwell time was 50 ms per step. An electron beam neutralizer was used during the XPS measurements. The Ar ion beam energy during depth profiling was 3 keV. The XPS data were collected using Auger Scan (RBD Instruments) software. The XPS data were analyzed employing CASA XPS (Casa Software Ltd.) software. All compositional data presented were collected by XPS after 60 s of Ar ion sputtering to remove atmospheric oxidation and adventitious C unless otherwise noted.

3. RESULTS AND DISCUSSION

3.1. TDMAT with NH_3, O_2, CH_4 and H_2 RBGs. Tetrakisdimethylamido Titanium(IV) (TDMAT) was used as the metal precursor to deposit EE-ALD films with NH_3, O_2, CH_4 and H_2 RBGs as shown in Figure 3. With the addition of the NH_3 RBG, high purity, low resistivity, crystalline TiN EE-ALD films were deposited at low temperatures as discussed in a previous publication.[23] The high purity TiN films illustrated the ability of the NH_3 RBG to remove carbon.[23] Low temperature crystallinity was also observed in the TiN EE-ALD films.[23]

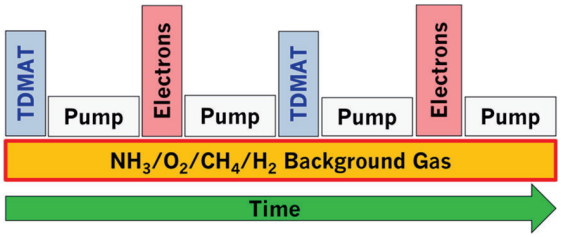

Figure 3. EE-ALD process for Ti-containing films using alternating TDMAT and electron exposures with continuous RBG.

3.1.1. TiO_2 EE-ALD Films. TiO_2 films are essential in many technological areas such as photocatalysis, solar energy conversion, gas sensors and optical coatings.[25] Figure 4a shows real-time in situ 4-wavelength ellipsometry of the TiO_2 EE-ALD film growth using TDMAT and O_2 RBG at temperatures <80 °C. The slight heating above room temperature was caused by the electron beam at an electron current of ~65 mA. The O_2 RBG pressure was 2 mTorr. 200 cycles of TiO_2 EE-ALD resulted in a ~150 Å thick film as measured by in situ 4-wavelength ellipsometry and ex situ

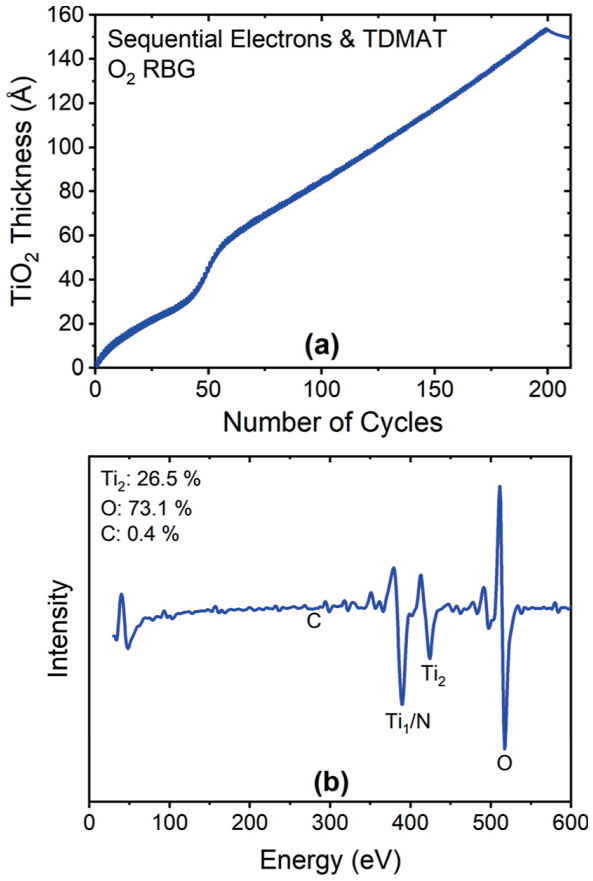

Figure 4. (a) In situ real-time 4-wavelength ellipsometry of TiO_2 nucleation and growth on a native oxide Si coupon. TiO_2 EE-ALD growth rate was 0.7 Å/cycle. (b) In vacuo AES showing C, Ti, Ti/N, and O AES signals for TiO_2 EE-ALD films grown on Si native oxide for a thickness of ~150 Å.

https://doi.org/10.1021/acs.chemmater.5c00264
Chem. Mater. 2025, 37, 4652−4664

spectroscopic ellipsometry. TiO_2 was deposited with a growth rate of ~0.7 Å/cycle.

TiO_2 EE-ALD using TDMAT and O_2 RBG displayed rapid nucleation. There was also a period of rapid increase in the derived TiO_2 thickness between cycles ~45 and ~55 in Figure 4a. This increase was reproducible and is likely caused by a change in film orientation or crystallinity as the TiO_2 film reached a critical thickness. Similar phenomena have been observed previously with TiO_2 ALD films at a thickness of 12 nm at temperatures of 150 and 260 °C.[26] TiO_2 crystallization can vary greatly based on interface quality, composition, and other factors.[27]

TiO_2 EE-ALD also produced ultrahigh purity films. The composition of the TiO_2 EE-ALD film was measured using in vacuo Auger electron spectroscopy (AES). Figure 4b reveals that the C signal was below the noise level indicating very low C content in the films. AES showed a near-stoichiometric, slightly oxygen-rich TiO_2 composition when using the Ti_2 peak for Ti quantification. Incomplete removal of the nitrogen-containing ligands of the TDMAT precursor could lead to N contamination in the films. AES was unable to differentiate between a potential N peak and the Ti_1 peak around 390 eV. Therefore, the Ti_2 peak was used to measure Ti. X-ray photoelectron spectroscopy (XPS) after surface sputtering identified no N or C in the bulk of the films as revealed by Figure S1, Supporting Information. Only a small N signal at ~1 at % was observed on the surface prior to sputtering.

The negligible N and C in the TiO_2 EE-ALD film is attributed to the creation of O radicals from the interaction of O_2 RBG and low energy electrons. The O radicals may scour the surface, reacting with C to form CO_x and N to form NO_x volatile compounds. The Ti centers may then react with either O_2 gas or O radicals to form TiO_2. XPS analysis showed a slightly O-rich film with a Ti/O ratio of 1:2.3. Excess oxygen may be incorporated into the film at grain boundaries or as interstitial excess oxygen defects.[28] Superstoichiometric incorporation of elements from RBGs have been observed previously with the incorporation of excess N in TiN EE-ALD films.[23]

Grazing incidence X-ray diffraction (GI-XRD) measured a small diffraction peak at $2\Theta = 25.4$. This peak corresponds to the TiO_2 [101] diffraction peak for tetragonal anatase.[29] EE-ALD with a RBG has previously been shown to lead to crystallinity during TiN EE-ALD.[23] The low energy electrons may lead to electron stimulated mobility of surface atoms that produce crystallinity at low temperatures. A TiO_2 EE-ALD film density of 3.89 g/cm^3 was extracted from the XRR measurements. This TiO_2 density corresponds well to the bulk value of ~3.9 g/cm^3 for anatase TiO_2.

Ex situ AFM analysis measured the RMS roughness for a TiO_2 EE-ALD film with a thickness of 150 Å. This TiO_2 EE-ALD film had an RMS roughness of ~8 Å over a 1 × 1 μm^2 area as shown in Figure S2, Supporting Information. Ex situ spectroscopic ellipsometry measurements were also able to model the optical bandgap of the TiO_2 film. The optical bandgap was found to be ~2.85 eV. This bandgap is lower than the literature value for the bandgap of anatase at 3.2 eV.[28] This lower bandgap may be due to the excess oxygen in the film. Oxygen-rich TiO_2 has been shown to have extra photochemical activity. This activity may be related to the bandgap narrowing caused by excess oxygen defects.[28,30]

3.1.2. Other Ti-Containing EE-ALD Films. Other Ti-containing EE-ALD films were deposited at T < 100 °C using CH_4 and H_2 RBGs. TiC EE-ALD was investigated using TDMAT with CH_4 RBG. The steady state growth rate was 2.3 Å/cycle. However, the films were not high purity TiC. XPS studies measured ~10 at % N incorporation in the films. XPS analysis also revealed a large O signal of 25 at %. This O incorporation in the film is likely from ex situ oxidation during air exposure prior to the XPS measurements.

TDMAT with H_2 RBG was also employed to deposit a $Ti_xN_yC_z$ EE-ALD film with a growth rate of 2.2 Å/cycle. XPS measurements after surface sputtering revealed a film composition of Ti at 31 at %, C at 23 at %, O at 23 at % and N at 22 at %. In contrast, in vacuo AES measurements revealed only a small oxygen signal. The in vacuo oxygen content is not exact due to the Ti/N AES peak overlap. However, the O content is estimated to be <6%. The large difference between the in vacuo AES and ex situ XPS O concentrations could indicate that the films were highly susceptible to atmospheric oxidation. A $Ti_xN_yC_z$ EE-ALD film with a thickness of 190 Å also had a surface RMS roughness of ~14 Å as measured by AFM.

3.2. Si_2H_6 with NH_3, O_2, CH_4, and H_2 RBGs. Si_2H_6 was employed as the metalloid precursor to deposit Si-containing EE-CVD films at low temperature T < 100 °C using repeating Si_2H_6 pulses together with a continuous electron beam and NH_3, O_2, CH_4 and H_2 RBGs as shown in Figure 5. EE-CVD

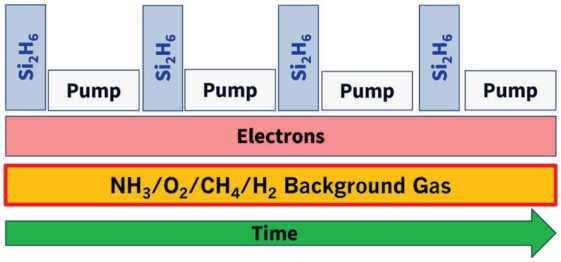

Figure 5. EE-CVD process for Si-containing films using continuous electron and RBG exposures and repeating Si_2H_6 pulses.

films can be deposited much more quickly than EE-ALD films. The faster deposition allows for more rapid prototyping of materials. Si_2H_6 provides the Si element. The various RBGs supply the second element to form the Si compounds. This strategy simplifies the growth of Si-containing films to employing Si_2H_6 for Si and easily accessible RBGs with high vapor pressure to provide the second element.

3.2.1. Si_3N_4 EE-CVD Films. Si_3N_4 films are useful as insulating and barrier materials in semiconductor devices. They also have wear, high temperature, and corrosion resistance. Figure 6a shows the deposition of Si_3N_4 films by EE-CVD with repeating Si_2H_6 pulses and an NH_3 RBG at T < 107 °C. The electron beam current was ~52 mA. The NH_3 RBG pressure was 2 mTorr. 300 Si_2H_6 pulses during Si_3N_4 EE-CVD resulted in a ~150 Å thick film. Si_3N_4 was deposited with a growth rate of 0.5 Å per Si_2H_6 pulse. In vacuo AES analysis of this film shown in Figure 6b was consistent with high purity, near stoichiometric Si_3N_4. The C and O AES peaks were in the noise.

Ex situ XPS analysis also revealed a stoichiometric Si/N ratio of 3:4 with a C impurity of 0.5 at % and an O impurity of 2 at %. The small C and O XPS signals probably result from reactor contamination because there is no C or O in the Si_2H_6 precursor or NH_3 RBG. The Si_3N_4 films were extremely

https://doi.org/10.1021/acs.chemmater.5c00264
Chem. Mater. 2025, 37, 4652−4664

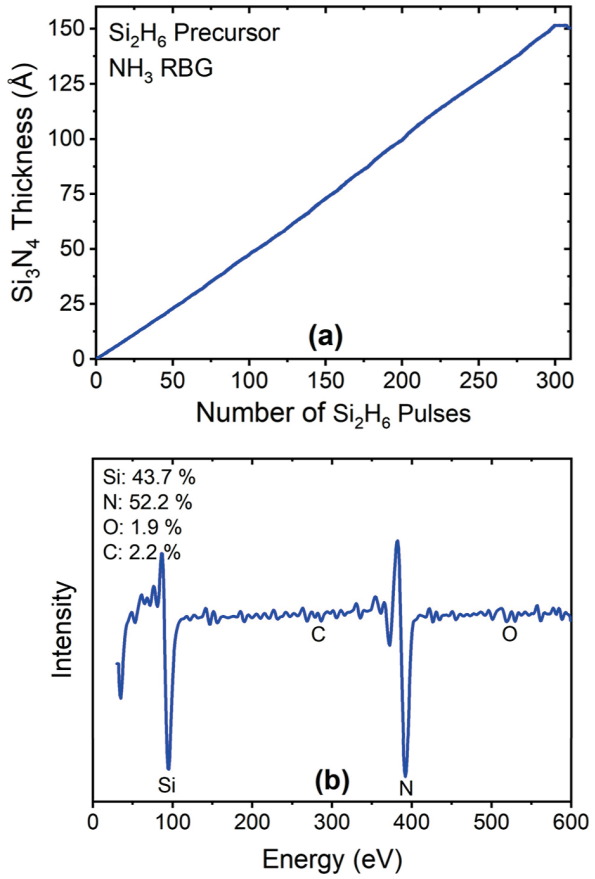

Figure 6. (a) In situ real-time 4-wavelength ellipsometry of Si_3N_4 nucleation and growth on a native oxide Si coupon. Si_3N EE-CVD growth rate was 0.5 Å per Si_2H_6 pulse. (b) In vacuo AES showing Si, C, N, and O AES signals for Si_3N_4 EE-CVD films grown on Si native oxide for a thickness of ∼150 Å.

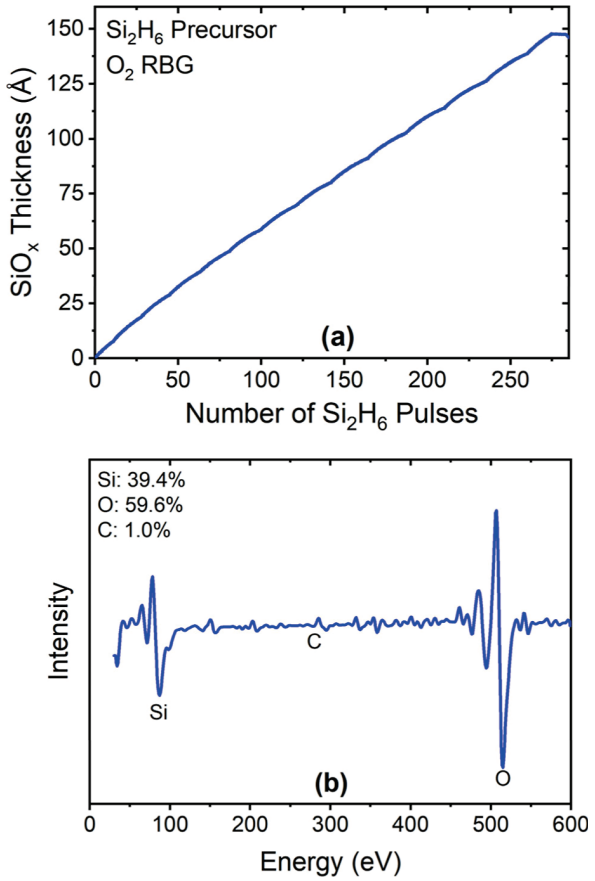

Figure 7. (a) In situ real-time 4-wavelength ellipsometry of SiO_x nucleation and growth on a native oxide Si coupon. SiO_x EE-CVD growth rate was 0.5 Å per Si_2H_6 pulse. (b) In vacuo AES showing Si, C, and O AES signals for SiO_x EE-CVD films grown on Si native oxide for a thickness of ∼150 Å.

smooth as deposited with an RMS surface roughness of ∼1 Å for a film thickness of 152 Å. Ex situ spectroscopic ellipsometry analysis also determined an optical bandgap of 5.2 eV near the reported value of ∼5 eV.[31] No crystallinity was detected in the Si_3N_4 EE-CVD films.

3.2.2. SiO_x EE-CVD Films. SiO_2 films function as insulating layers in semiconductor devices and also have critical applications as optical coatings. SiO_2 EE-ALD films were deposited earlier using Si_2H_6 together with O_3 or H_2O as the second reactant.[6] In this study, SiO_x EE-CVD films were successfully grown using EE-CVD with Si_2H_6 pulses and O_2 RBG at T < 100 °C. The electron beam current was ∼35 mA. The O_2 RBG pressure was 2 mTorr. Figure 7a shows that 275 Si_2H_6 repeating pulses during SiO_x EE-CVD resulted in a ∼150 Å thick film. SiO_x films were deposited with a growth rate of 0.5 Å per Si_2H_6 pulse during SiO_x EE-CVD. In terms of composition, XPS analysis yielded a Si/O ratio of 1:1 in the film bulk and a surface ratio of 1:1.2 prior to Ar^+ ion sputtering.

The in vacuo AES measurements shown in Figure 7b also yield a Si/O ratio of 1:1.5. However, the films may be closer to stoichiometric SiO_2 because an ex situ spectroscopic ellipsometry model for a thermal Si oxide[32] fit the ellipsometry results very well without modification. Si-rich SiO_2 films also have larger indices of refraction that were not observed for the SiO_x EE-CVD films.[33] In addition, no crystallinity was observed in the SiO_x EE-CVD films. The SiO_x films were also extremely smooth with an RMS surface roughness of ∼1 Å as measured by AFM for films with a thickness of 148 Å.

3.2.3. SiC_x EE-CVD Films. SiC films are vital in power electronics devices.[34] However, SiC CVD is a high temperature process requiring temperatures around 950−1330 °C.[35−37] Si_2H_6 pulses together with continuous electron exposures and CH_4 RBG were used to grow SiC_x EE-CVD films at much lower temperatures. Figure 8a shows that 500 Si_2H_6 pulses were used to deposit a ∼203 Å thick film. This SiC_x film was very smooth as measured by AFM with an RMS surface roughness of ∼1 Å as displayed in Figure S3, Supporting Information. The SiC_x EE-CVD films grew linearly with repeating Si_2H_6 pulses at a growth rate of 0.4 Å per Si_2H_6 pulse.

The SiC_x EE-CVD growth occurred at temperatures <100 °C resulting from electron beam heating of the sample with an electron beam current of ∼50 mA. The CH_4 RBG pressure in Figure 8a was 0.45 mTorr as measured by the cold cathode pressure gauge in an otherwise empty chamber pumped by the turbomolecular pump. Changing the pressure of the Si_2H_6 pulses also affected the deposition rate resulting from the CVD-like nature of EE-CVD.

The composition of the SiC_x EE-CVD film was measured using in vacuo AES in Figure 8b. The AES results yielded a Si/C ratio of 1:1.3. The O signal was below the noise level

https://doi.org/10.1021/acs.chemmater.5c00264
Chem. Mater. 2025, 37, 4652−4664

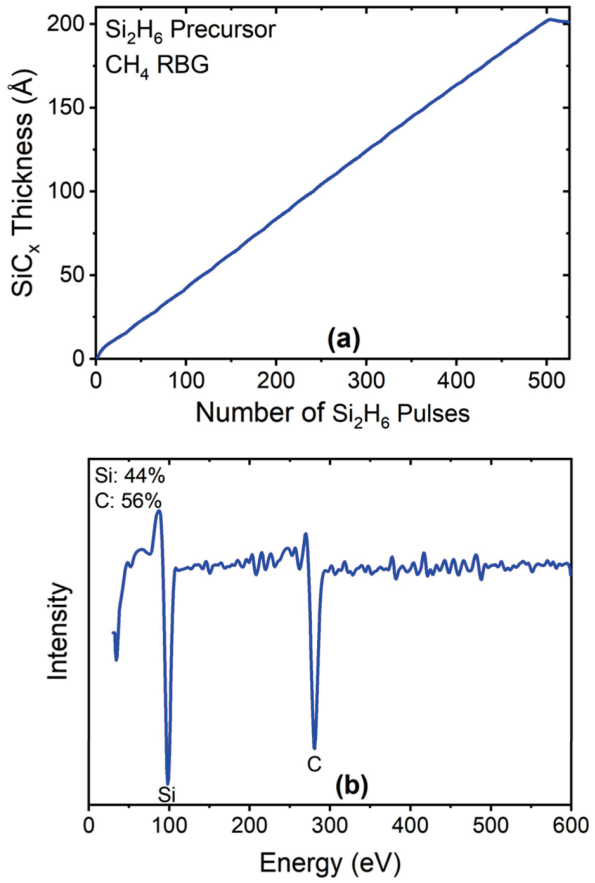

Figure 8. (a) In situ real-time 4-wavelength ellipsometry of SiC_x nucleation and growth on a native oxide Si coupon. SiC_x EE-CVD growth rate was 0.4 Å per Si_2H_6 pulse. (b) In vacuo AES showing Si and C AES signals for SiC_x EE-CVD films grown on Si native oxide for a thickness of ∼200 Å.

indicating very low O content. XPS results after Ar^+ ion sputtering were consistent with a near perfect Si/C ratio of 1:1 and a small 3 at % O impurity as demonstrated by Figure S4, Supporting Information. The small discrepancy between the AES and XPS results may be attributed to C deposition on the top of the SiC_x film from the CH_4 interaction with the electron beam after the Si_2H_6 pulsing stopped and before the CH_4 RBG was turned off. Additional AES measurements revealed the deposition of a pure C film from the interaction between the CH_4 RBG and the low energy electron beam. There was no crystallinity monitored in the SiC_x EE-CVD films.

The CH_4 pressure must be carefully controlled during SiC_x EE-CVD. Excess CH_4 introduced into the chamber during EE-CVD will be decomposed by the electron beam and deposited as C on the sample. An identical experiment to that shown in Figure 8a was conducted with a CH_4 RBG pressure of 1.0 mTorr for 400 Si_2H_6 pulses. The Si/C ratio measured by XPS after this experiment was 1:5. The C deposition rate is greater with the increased CH_4 RBG pressure. In addition, the film thickness was ∼40 nm. This thickness was twice the thickness of the film grown with a CH_4 pressure of 0.45 mTorr despite being deposited with 20% fewer pulses. In addition, the film roughness also changed for the larger CH_4 RBG pressure. The carbon-rich was significantly rougher than the film grown in Figure 8a with an RMS roughness of 7 Å for a film with a thickness of 398 Å. Rapid C EE-CVD from the CH_4 RBG may cause the increased film roughness.

3.2.4. SiH_x EE-CVD Films. Silicon films have many essential applications in semiconductor devices, photovoltaics and photonics. SiH_x EE-CVD films were grown with Si_2H_6 pulses and H_2 RBG. A Si wafer with a 1 μm thick TiN layer on the surface was used to measure the deposited SiH_x film. Figure 9a

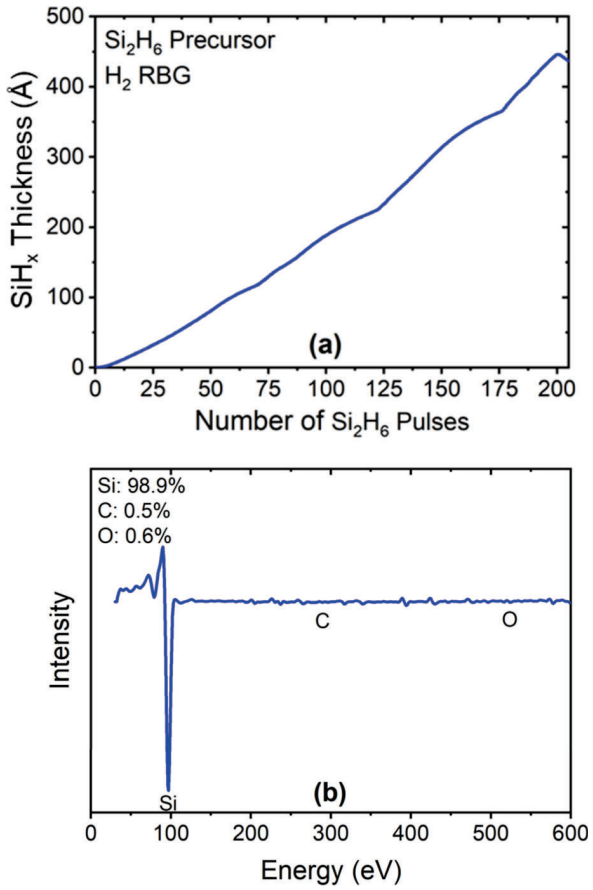

Figure 9. (a) In situ real-time 4-wavelength ellipsometry of SiH_x nucleation and growth on 1 μm TiN film on a Si coupon. SiH_x EE-CVD growth rate was 2.2 Å per Si_2H_6 pulse. (b) In vacuo AES showing Si, C, and O AES signals for SiH_x EE-CVD films grown on 1 μm TiN film on a Si coupon for a thickness of ∼450 Å.

shows the growth of SiH_x EE-CVD film at $T < 100$ °C using an electron beam current of ∼58 mA. The H_2 RBG pressure was 2 mTorr. A SiH_x film with a thickness of 446 Å was deposited by the 200 Si_2H_6 pulses. The growth rate was 2.2 Å per Si_2H_6 pulse. The SiH_x EE-CVD films were very pure. Figure 9b shows the in vacuo AES results for the film grown in Figure 9a. In vacuo AES was not able to discern an O or C signal above the baseline noise. After Ar^+ sputtering, ex situ XPS analysis measured an 8.5 at % O impurity, likely from ex situ oxidation. There was also a small C impurity of <2 at % probably from reactor or atmospheric contamination.

The SiH_x EE-CVD films were also analyzed using ex situ spectroscopic ellipsometry. A Tauc-Lorentz model for a-Si was employed as a starting point. The optical bandgap was measured at ∼1.6 eV consistent with a-Si/H.[38] Modulation of the H_2 RBG pressure may lead to different bandgaps due to different amounts of H inclusion in the SiH_x film. SiH_x EE-CVD films could be grown without the H_2 RBG. The H_2 RBG

https://doi.org/10.1021/acs.chemmater.5c00264
Chem. Mater. 2025, 37, 4652−4664

was included to assist in the removal of any contamination from the SiH_x film.

Separate studies revealed that the combination of low energy electrons and H_2 RBG was able to etch the SiH_x surface. The probable etch product is SiH_4.[39,40] However, greater SiH_x deposition was able to overcome this competitive Si etch. The Si_2H_6 pressure behind the micropulse valve was 2 Torr. This pressure is twice the pressure used for deposition of the other Si-containing EE-CVD films. Additionally, the valve was actuated for 0.500 s, 5× longer than for the deposition of the other Si-containing films. The SiH_x EE-CVD films had an RMS surface roughness of ∼27 Å as measured by AFM for films with a thickness of 446 Å. No crystallinity was detected in the SiH_x EE-CVD films.

3.3. $W(CO)_6$ with NH_3, O_2, CH_4, and H_2 RBGs. Various W-containing EE-CVD films were deposited using $W(CO)_6$ as the metal precursor together with NH_3, O_2, CH_4, and H_2 RBGs as shown in Figure 10. There is no known thermal

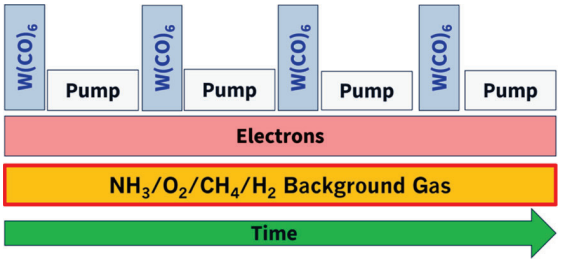

Figure 10. EE-CVD process for W-containing films using continuous electron and RBG exposures and repeating $W(CO)_6$ pulses.

decomposition of $W(CO)_6$ at the low temperatures of T < 120 °C which results from electron beam heating of the samples.[41] $W(CO)_6$ will undergo dissociative electron attachment to produce $W(CO)_x^-$ anions with x = 2−5 at low electron energies from 1 to 14 eV that are typical for secondary electrons.[42]

3.3.1. W_2N EE-CVD Films. W_2N films are important as diffusion barriers and protective coatings.[43] $W(CO)_6$ with NH_3 RBG led to W_2N EE-CVD. In situ ellipsometry measurements of W_2N EE-CVD film growth is displayed in Figure 11a at T < 120 °C with an electron current of ∼73 mA. The NH_3 RBG pressure was 2 mTorr. 575 $W(CO)_6$ pulses resulted in a film thickness of ∼115 Å. These results yield a growth rate of ∼0.17 Å per $W(CO)_6$ pulse. The results show that W_2N EE-CVD has rapid nucleation. In addition, the EE-CVD growth rate increased slightly during deposition. This increase could be caused by the sample heating slowly during the deposition. The sample temperature started at room temperature and increased to ∼100 °C resulting from electron beam heating.

The film resistivity was also determined in Figure 11a by the in situ 4-wavelength ellipsometry measurements using a Drude-Lorentz model.[7] The initial resistivity was high for film thicknesses <20 Å. The resistivity reached a fairly constant value after ∼250 $W(CO)_6$ pulses. The final resistivity was 325 $\mu\Omega$·cm for a film thickness of ∼115 Å. Ex situ spectroscopic ellipsometry measurements on the same film yielded a film thickness of ∼125 Å. The ex situ spectroscopic ellipsometry measurements were also able to determine the film resistivity. These measurements yielded a resistivity of 469 $\mu\Omega$·cm. The in situ 4-wavelength and ex situ spectroscopic ellipsometry measurements are in fair agreement especially considering

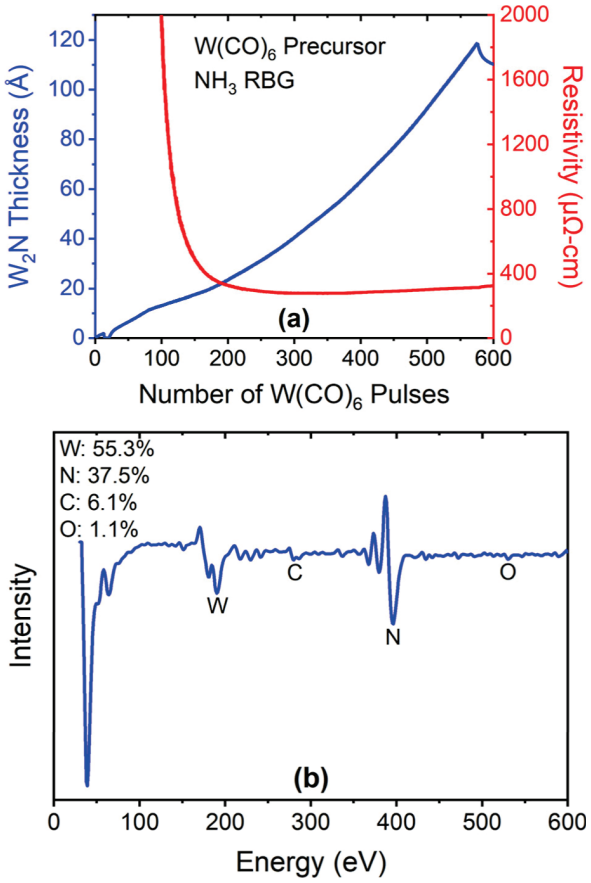

Figure 11. (a) In situ real-time 4-wavelength ellipsometry of W_2N nucleation and growth on a Si native oxide coupon. W_2N EE-CVD growth rate was 0.17 Å per $W(CO)_6$ pulse. (b) In vacuo AES showing W, C, N, and O AES signals for W_2N EE-CVD films grown on a Si native oxide coupon for a thickness of ∼115 Å.

the possibility that ex situ oxidation may increase the film resistivity. Additionally, the 4 wavelength ellipsometer used for the in situ 4-wavelength ellipsometry measurements had to extrapolate the Drude oscillator amplitude due to the limited number of wavelengths.

The composition of the W_2N EE-CVD films was also measured using in vacuo Auger electron spectroscopy (AES). Figure 11b shows high purity W_2N films with low C and O content at 6.1 at % and 1.1 at %, respectively. The O AES signal is very small and may be background noise. The AES results were consistent with a W/N ratio of 1:0.66 and a N-rich W_2N film. The low C content indicates that the CO ligand or C from CO dissociation is removed during W_2N EE-CVD. Ex situ AFM measurements determined that the RMS surface roughness was only ∼4 Å for the film thickness of 90 Å as displayed in Figure S5, Supporting Information.

Ex situ XPS analysis of the W_2N film in Figure 11a after Ar^+ sputtering also found no C or O XPS signals in the bulk of the film as shown in Figure S6, Supporting Information. The XPS results were consistent with a W/N ratio of 1:0.36. The higher W/N ratio after surface sputtering may be due to preferential N atom sputtering by the Ar^+ ion beam. The lack of C and O in the W_2N EE-CVD film is noteworthy because previous work on $W(CO)_6$ decomposition under electron bombardment showed the formation of tungsten oxides along with graphitic carbon.[44] In contrast, the addition of the NH_3 RBG in this

https://doi.org/10.1021/acs.chemmater.5c00264
Chem. Mater. 2025, 37, 4652−4664

study resulted in the complete removal of C and O from the films.

The interaction between the NH_3 RBG with the low energy electrons may create reactive $\bullet NH_2$ and $\bullet H$ species. These species may be responsible for the removal of possible C and O species from the W_2N EE-CVD films. In similarity to the earlier results for TiN EE-ALD, the $\bullet NH_2$ and $\bullet H$ species may remove C and O species by forming volatile CH_4, CH_3NH_2, NO_x or H_2O products.[23]

GI-XRD analysis was also conducted on the W_2N film grown in Figure 11a. Diffraction peaks were observed at 2θ = 37.4° and 44.1° and two smaller broad peaks at 2θ = 63.2° and 76° as shown in Figure S7, Supporting Information. These peaks fit extremely well with the W_2N XRD spectrum (PDF 00-25-1257).[45,46] This identification of the film as W_2N is also consistent with the compositional analysis. The W_2N EE-CVD film grown in Figure 11a was also modeled by XRR. A film density of 16.0 g/cm^3 was extracted from the model. In comparison, β-W_2N has a density of 17.97 g/cm^3 calculated from its crystallographic structure.[45]

Smooth, high density, low resistivity W_2N EE-CVD films may be useful as back-end-of-line diffusion barriers for metallization.[47,48] Metal−organic CVD (MOCVD) of WN at 500 °C showed C and O impurities at ca. 5% and a resistivity of 590 $\mu\Omega$·cm.[48] In comparison, the W_2N EE-CVD films in this work were deposited at <120 °C with C and O impurities below the XPS detection limit and displayed a resistivity of ~469 $\mu\Omega$·cm by SE. Additionally, the W_2N EE-CVD films were highly dense and ultrasmooth, both desirable properties in diffusion barriers.

3.3.2. WO_x EE-CVD Films. WO_3 films are useful for many applications in the areas of photochromism, photocatalysis and gas sensors.[49] WO_x EE-CVD films were grown using EE-CVD with $W(CO)_6$ pulses and O_2 RBG. Figure 12a shows the WO_x EE-CVD film growth as a function of the number of $W(CO)_6$ pulses at T < 95 °C with an electron current of 45 mA. The O_2 RBG pressure was 2 mTorr. 600 $W(CO)_6$ pulses resulted in a film thickness of ~300 Å. After an initial nucleation period, there is a steady state growth rate of 0.5 Å per $W(CO)_6$ pulse. There is also a significant change in growth rate and optical thickness observed by the real-time in situ 4-wavelength ellipsometry measurements around the 150th $W(CO)_6$ pulse. This reproducible behavior is likely caused by the transition from a thin amorphous film to a thicker crystalline film. The change in optical properties affects the optical model resulting in an increase in optical thickness. A similar transition was observed during the TiO_2 EE-ALD growth observed in Figure 4a.

The GIXRD spectra of the WO_x EE-CVD film show crystallinity and match the spectra for tetragonal WO_3 as displayed in Figure S8, Supporting Information.[50] This crystallinity is noteworthy because the tetragonal WO_3 phase is known to form above 1100 K.[50] The low energy electron beam may again supply sufficient atomic mobility for the crystallization in a high temperature phase at T < 100 °C. The optical bandgap of the WO_x EE-CVD films was also measured to be 3.0 eV by the ex situ spectroscopic ellipsometry measurements using a Tauc-Lorentz model. This bandgap is very near literature reports of WO_3 bandgaps of 3.05 eV.[51] In addition, the WO_x EE-CVD films were smooth with an RMS surface roughness of ~5.6 Å measured by AFM.

Figure 12b displays the in vacuo AES analysis of the WO_x EE-CVD film. The AES peaks are consistent with a W/O ratio

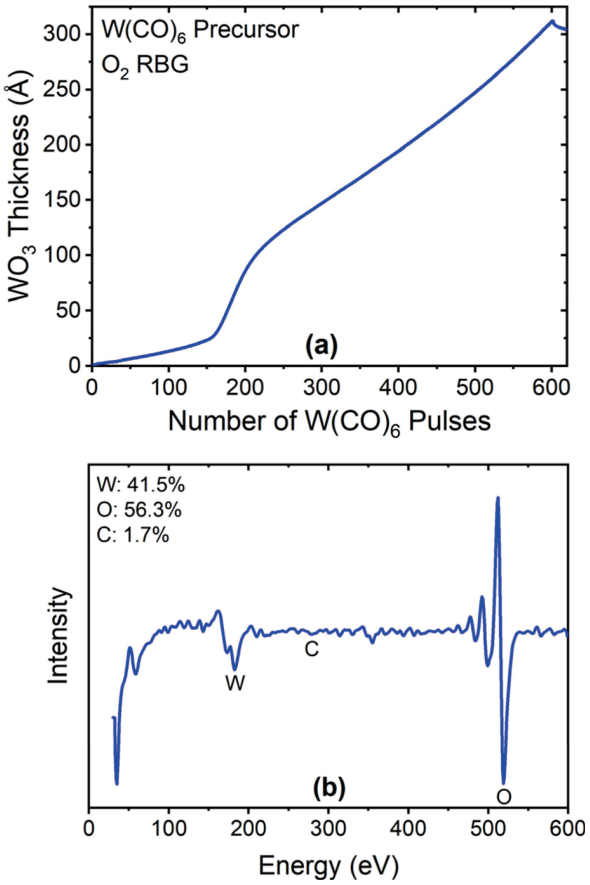

Figure 12. (a) In situ real-time 4-wavelength ellipsometry of WO_3 nucleation and growth on a Si native oxide coupon. WO_3 EE-CVD growth rate was 0.5 Å per $W(CO)_6$ pulse. (b) In vacuo AES showing W, C, and O AES signals for WO_3 EE-CVD films grown on a Si native oxide coupon for a thickness of ~300 Å.

of ~1:1.35 with no C AES signal discernible above the noise level. XPS analysis after Ar^+ sputtering also detected no C in the WO_x films grown by EE-CVD. No C is consistent with C removal by O radicals or the complete removal of CO ligands from $W(CO)_6$ by ESD. After surface sputtering, XPS analysis also reveals that the W/O ratio is 1:1.3. This ratio is different than the W/O ratio of 1:2.1 from the XPS surface scan. This lower ratio may be due to preferential sputtering of O from WO_3 films during sputtering.[52] However, this W/O ratio also agrees well with the in vacuo AES measurements. These W/O ratios are not in agreement with the 1:3 ratio expected from the crystal structure and optical bandgap results.

3.3.3. WC_x EE-CVD Films. Tungsten carbide films have high hardness and are important for diffusion barriers and wear-resistance coatings.[53] $W(CO)_6$ was used as a metal precursor together with a CH_4 RBG for WC_x EE-CVD. WC_x EE-CVD growth versus number of $W(CO)_6$ pulses is shown in Figure 13a at T < 110 °C with an electron current of 56 mA. The 400 repeating $W(CO)_6$ pulses resulted in a film thickness of ~283 Å. The steady state growth rate was 0.46 Å per $W(CO)_6$ pulse with a CH_4 RBG pressure of 3×10^{-5} Torr. Corresponding in vacuo AES results displayed in Figure 13b yielded a W/C ratio of 1:0.8. For higher CH_4 pressures of 1×10^{-4}, the growth rate was 0.71 Å per $W(CO)_6$ pulse with a W/C ratio was 1:1.4. As the CH_4 pressure was increased further to 5×10^{-4} Torr, the

https://doi.org/10.1021/acs.chemmater.5c00264
Chem. Mater. 2025, 37, 4652−4664

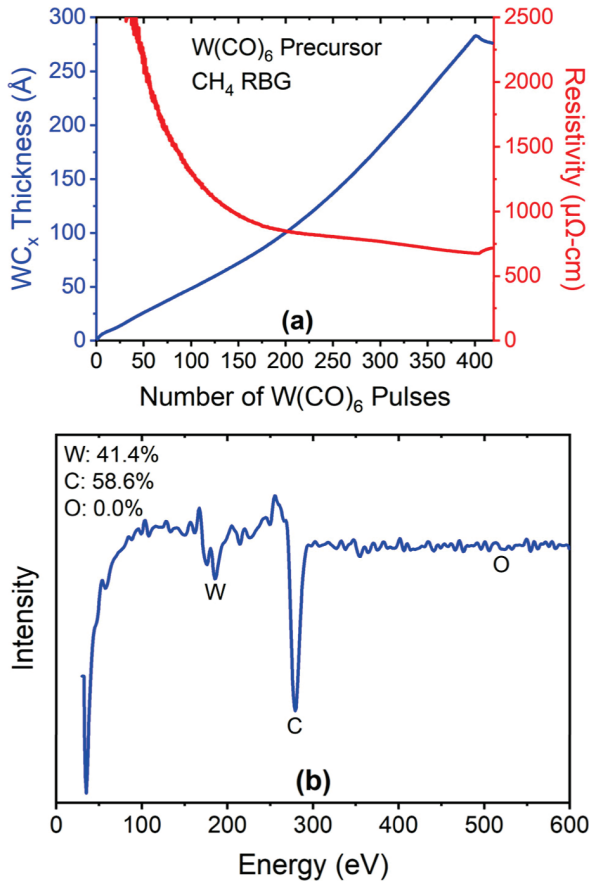

Figure 13. (a) In situ real-time 4-wavelength ellipsometry of WC_x nucleation and growth on a Si native oxide coupon. WC_x EE-CVD growth rate was 0.46 Å per $W(CO)_6$ pulse. (b) In vacuo AES showing W, C, and O AES signals for WC_x EE-CVD films grown on a Si native oxide coupon for a thickness of ~283 Å.

W/C ratio was 1:2.3 and the growth rate increased to 0.76 Å per $W(CO)_6$ pulse.

The WC_x films were high purity as determined by AES and XPS. All three films grown at CH_4 pressures of 3×10^{-5} Torr, 1×10^{-4} Torr and 5×10^{-4} Torr, had an O content of 4% or less. The O content was slightly lower at the higher CH_4 pressures. Additionally, all three films displayed diffraction patterns consistent with the metastable cubic β-WC_{1-x} pattern (PDF 04-022-5716) as revealed in Figure S9, Supporting Information.[54,55] In addition, the WC_x films were smooth as measured by AFM. The RMS surface roughnesses were ~7, 5, and 10 Å in increasing order of C content.

The film resistivity was also determined in Figure 13a by the in situ 4-wavelength ellipsometry measurements using a Drude-Lorentz model. The initial resistivity was high for film thicknesses <20 Å. The resistivity decreased versus thickness and began to reach a constant value around ~150 $W(CO)_6$ pulses. The final resistivity was ~750 $\mu\Omega$·cm for a film thickness of ~275 Å. Ex situ spectroscopic ellipsometry measurements on the same film determined a film thickness of 327 Å. The ex situ spectroscopic ellipsometry measurements yielded a resistivity of 702 $\mu\Omega$·cm in good agreement with the in situ 4-wavelength ellipsometry measurements.

3.3.4. Other W-Containing EE-CVD Films. An attempt was made to deposit W EE-CVD films using $W(CO)_6$ pulses together with H_2 RBG. In situ 4-wavelength ellipsometry measurements observed film growth at 0.4 Å per $W(CO)_6$ pulse. However, XPS analysis after Ar^+ sputtering measured a C residue in the films at ~20 at % with a small O impurity of ~2 at %. The H radicals generated from the interaction of the H_2 RBG and low energy electrons were not sufficient to remove C from the films. However, the films were crystalline with a β-WC_{1-x} XRD pattern (PDF 04-022-5716) and an RMS roughness of 1.4 nm.

Such a low C content and an WC_x XRD phase identification suggests an amorphous W metal film with WC crystallites. Ex situ spectroscopic ellipsometry measurements also yielded a film resistivity of 230 $\mu\Omega$·cm that was consistent with substantial metallic character. XRR measurements of the film density yielded a value of 16.8 g/cm^3 compared to the literature value for W of 19.3 g/cm^3.[56] The slightly lower density than W likely results from the C impurity. Lastly, these EE-CVD films had an RMS surface roughness of ~14 Å measured by AFM for films with a thickness of 283 Å.

3.4. Overview and Future Outlook. This survey has demonstrated the deposition of many Ti-, Si- and W-containing films at low temperatures using electron-enhanced processing with RBGs. The success of this methodology is attributed to the interaction of the electrons with the RBG to form radical species that can react with the surface of the growing film. These radical species act in concert with the metal or metalloid precursors to grow the films and improve film purity. The incident electron beam flux on the surface also keeps active sites available by electron stimulated desorption of ligands from surface sites. The radical species and electron stimulated desorption facilitate rapid nucleation, low temperature growth and high purity films.

The survey has also illustrated that simple, highly volatile metal or metalloid precursors can react with various RBGs to form a wide range of compounds at low temperatures. Comparisons between the temperatures for thermal and electron-enhanced growth for SiC can help illustrate the advantages of electron-enhanced processing. SiC thermal CVD was performed at 1330 °C using $SiH_4 + C_3H_8$,[36] at 1200−1350 °C using CH_3SiCl_3,[37] and at 950−1000 °C using $SiCl_4 + C_2H_4$.[35] SiC thermal ALD was obtained at 1000−1050 °C using $Si_2H_6 + C_2H_2$,[57] or at 850−980 °C using $Si_2H_6 + C_2H_4$.[58] In contrast, SiC EE-CVD was accomplished in this study using Si_2H_6 and CH_4 at much lower temperatures <100 °C.

There are also large differences between the temperatures for thermal and electron-enhanced growth for W_2N. W_2N thermal CVD occurs at growth temperatures between 250 and 500 °C using $W(CO)_6$ and NH_3.[48] W_2N thermal ALD is also obtained at temperatures from 327 to 527 °C using WF_6 and NH_3.[46] In contrast, W_2N EE-CVD was achieved in this study using $W(CO)_6$ and NH_3 at lower temperatures <120 °C.

The general EE-ALD and EE-CVD schemes shown in Figure 1 could be applied to grow many other film compositions using various metal or metalloid precursors and different RBGs. Other volatile metal or metalloid precursors are possible such as hydride, halide, carbonyl, amido, and alkyl complexes. Examples include GeH_4, $HfCl_4$, $Ni(CO)_5$, $Al(N(CH_3)_2)_3$ and $Ga(CH_3)_3$. Other volatile hydride RBGs are also possible such as H_2S, B_2H_6, H_2Se, PH_3, and AsH_3 for the deposition of sulfides, borides, selenides, phosphides and arsenides, respectively.

For example, sulfides like WS_2 or MoS_2 could be grown with a $W(CO)_6$ or $Mo(CO)_6$ metal precursor and an H_2S RBG. These transition metal dichalcogenides (TMDs) are a

https://doi.org/10.1021/acs.chemmater.5c00264
Chem. Mater. 2025, 37, 4652−4664

promising class of materials due to their favorable electronic properties.[59] However, the deposition of high-quality TMD films by CVD requires high temperatures.[60] EE-ALD or EE-CVD may allow for TMD deposition at low temperatures.

Carbides such as HfC and ZrC could also be grown with $HfCl_4$ or $ZrCl_4$ metal precursors and a CH_4 RBG. These carbides are important hard, refractory materials with potential uses as wear resistant coatings and protective material in hypersonic environments.[61,62] Low temperature deposition by EE-CVD may increase the use of these materials because the temperatures needed for HfC and ZrC CVD are >1000 °C.[63,64]

Metal borides could be grown by EE-CVD using various metal precursors together with diborane (B_2H_6) RBG. For example, TiB_2 films could be grown with $Ti(N(CH_3)_2)_3$ as the metal precursor together with a B_2H_6 RBG. Metal borides are refractory materials with high hardness and applications in catalysis, energy storage, and thermal protection systems.[65−67] However, the temperature required for the CVD of metal borides such as TiB_2 is around 900 °C.[68,69] EE-CVD techniques could significantly reduce this required growth temperature to T < 100 °C.

Ternary materials may also be deposited using EE-CVD techniques. Next generation Cu diffusion barriers for backend interconnects may require ternary materials.[70,71] Ternaries could be deposited using two RBGs together with a metal or metalloid precursor. For example, TiCN barriers could be deposited by EE-CVD using $Ti(N(CH_3)_2)_3$ together with NH_3 and CH_4 RBGs. The rapid nucleation and smooth surfaces obtained using EE-CVD techniques may be especially important for ultrathin ternary diffusion barriers.

4. CONCLUSIONS

EE-ALD and EE-CVD can be used for the low temperature growth of various titanium, silicon, and tungsten-containing films with TDMAT, Si_2H_6 and $W(CO)_6$, respectively, as the metal or metalloid precursors in the presence of different RBGs. EE-ALD occurs with alternating precursor and electron exposures. EE-CVD occurs with repeating precursor pulses and a continuous electron beam exposure. For both EE-ALD and EE-CVD, the continuous RBG helps to form high purity films. The O_2, NH_3 and CH_4 RBGs were observed to form oxides, nitrides and carbides with the various metal or metalloid precursors.

EE-ALD employs electrons as a reactant in the ALD process. TiO_2 EE-ALD was demonstrated using alternating exposures of TDMAT and low energy electrons with a continuous O_2 RBG. TiO_2 EE-ALD films displayed linear growth versus TDMAT and electron cycles. The TiO_2 EE-ALD films were deposited at a growth rate of ∼0.7 Å/cycle with no impurities at temperatures <80 °C. The TiO_2 films were smooth, crystalline and had an optical bandgap of 2.85 eV. Other Ti-containing films were deposited using NH_3, CH_4 and H_2 RBGs.

EE-CVD changes the role of the electrons from a periodically dosed reactant in EE-ALD to the role of a continuously dosed reactant in EE-CVD. In EE-CVD, both the electrons and RBG are continuously present and the precursors are pulsed repeatedly to control the film growth. Various silicon-containing films were deposited including Si_3N_3, SiO_2, SiC_x, and SiH_x with Si_2H_6 as the metalloid precursor. Various tungsten-containing films were deposited including W_2N, WO_x, and WC_x with $W(CO)_6$ as the metal precursor. These films all displayed linear growth versus the number of repeating precursor pulses at low temperature.

The Si_3N_4 and SiO_x EE-CVD films both grew immediately and linearly versus number of Si_2H_6 pulses at a growth rate of 0.5 Å per Si_2H_6 pulse with either NH_3 or O_2 RBGs, respectively. The growth rate and composition of the SiC_x EE-CVD films was dependent on the pressure of the CH_4 RBG because higher CH_4 pressures led to increased C EE-CVD. SiH_x EE-CVD films also grew immediately and linearly versus number of Si_2H_6 pulses at a growth rate of 2.2 Å per Si_2H_6 pulse with a H_2 RBG. The SiH_x EE-CVD films had high purity and a bandgap of ∼1.6 eV consistent with a-Si/H. All the silicon-containing EE-CVD films were amorphous according to XRD studies.

Using $W(CO)_6$ as the metal precursor, W_2N, WO_x, and WC_x EE-CVD films were deposited using NH_3, O_2 and CH_4 RBGs, respectively. The W_2N EE-CVD films were deposited at a growth rate of ∼0.17 Å per $W(CO)_6$ pulse. The W_2N EE-CVD films displayed crystallinity consistent with cubic W_2N. The W_2N films also displayed low resistivity of ∼450 $\mu\Omega$ cm and were very smooth as measured by AFM. The WO_x EE-CVD films were deposited at a growth rate of 0.5 Å per $W(CO)_6$ pulse. The crystallinity of these films was consistent with tetragonal WO_3. The optical bandgap of 3.0 eV also confirmed the WO_3 assignment. WC_x EE-CVD were also deposited with a composition dependent on the pressure of the CH_4 RBG. The growth rate for WC_x EE-CVD films with a W/C ratio of 1:0.8 was 0.46 Å per $W(CO)_6$ pulse. The growth rate increased as more carbon was incorporated at higher CH_4 pressures. The WC_x EE-CVD films with a W/C ratio of 1:0.8 had a low resistivity of ∼750 $\mu\Omega$ cm. All the WC_x EE-CVD films displayed diffraction patterns consistent with metastable cubic β-WC_{1-x}.

These studies illustrate that a broad range of films can be deposited at low temperatures using electrons together with simple metal or metalloid precursors and various RBGs. In addition to the nitrides, oxides and carbides demonstrated in these investigations, many other metal or metalloid precursors and RBGs are possible to deposit sulfides, phosphides and borides. The combination of several RBGs may also allow for the deposition of ternary films. Electron-enhanced processing with various metal or metalloid precursors and RBGs should extend the range of thin films that can be deposited at low temperatures.

■ ASSOCIATED CONTENT

Supporting Information

The Supporting Information is available free of charge at https://pubs.acs.org/doi/10.1021/acs.chemmater.5c00264.

XPS survey spectra of TiO_2 EE-ALD, SiC EE-CVD and W_2N EE-CVD films after Ar sputtering. AFM scans of TiO_2 EE-ALD, SiC EE-CVD and W_2N EE-CVD films. GI-XRD scans of W_2N, WO_x and WC_{1-x} EE-CVD films (PDF)

■ AUTHOR INFORMATION

Corresponding Author

Steven M. George − *Department of Chemistry, University of Colorado, Boulder, Colorado 80309-0215, United States;* orcid.org/0000-0003-0253-9184;
Email: Steven.George@Colorado.edu

https://doi.org/10.1021/acs.chemmater.5c00264
Chem. Mater. 2025, 37, 4652−4664

Authors

Zachary C. Sobell − *Department of Chemistry, University of Colorado, Boulder, Colorado 80309-0215, United States*

Andrew S. Cavanagh − *Department of Chemistry, University of Colorado, Boulder, Colorado 80309-0215, United States;* orcid.org/0000-0002-6201-530X

Complete contact information is available at: https://pubs.acs.org/10.1021/acs.chemmater.5c00264

Notes

The authors declare no competing financial interest.

■ ACKNOWLEDGMENTS

This work was supported by the Joint University Microelectronics Program (JUMP) funded by the Semiconductor Research Corporation (SRC). The authors acknowledge Rebecca Hirsch for the GI-XRD measurements. The authors also thank Blaine Johs from Filmsense and Marcel Junige for fruitful discussions regarding ellipsometric modeling. The authors would also like to acknowledge Kenneth Smith and Don David from the University of Colorado Integrated Instrument Development Facility for their construction and maintenance of the HC-PES and computer interfacing.

■ REFERENCES

(1) Sobell, Z. C.; Cavanagh, A. S.; Boris, D. R.; Walton, S. G.; George, S. M. Hollow Cathode Plasma Electron Source for Low Temperature Deposition of Cobalt Films by Electron-Enhanced Atomic Layer Deposition. *J. Vac. Sci. Technol., A* **2021**, *39*, 042403.

(2) Sobell, Z. C.; Cavanagh, A. S.; George, S. M. Growth of Cobalt Films at Room Temperature Using Sequential Exposures of Cobalt Tricarbonyl Nitrosyl and Low Energy Electrons. *J. Vac. Sci. Technol., A* **2019**, *37*, 060906.

(3) Sprenger, J. K.; Cavanagh, A. S.; Sun, H.; Wahl, K. J.; Roshko, A.; George, S. M. Electron Enhanced Growth of Crystalline Gallium Nitride Thin Films at Room Temperature and 100°C Using Sequential Surface Reactions. *Chem. Mater.* **2016**, *28*, 5282−5294.

(4) Sprenger, J. K.; Sun, H.; Cavanagh, A. S.; George, S. M. Electron-Enhanced Atomic Layer Deposition of Silicon Thin Films at Room Temperature. *J. Vac. Sci. Technol., A* **2017**, *36*, 01A118.

(5) Sprenger, J. K.; Sun, H.; Cavanagh, A. S.; Roshko, A.; Blanchard, P. T.; George, S. M. Electron-Enhanced Atomic Layer Deposition of Boron Nitride Thin Films at Room Temperature and 100°C. *J. Phys. Chem. C* **2018**, *122*, 9455−9464.

(6) Gertsch, J. C.; Sobell, Z. C.; Cavanagh, A. S.; Simka, H.; George, S. M. Electron-Enhanced SiO_2 Atomic Layer Deposition at 35 °C Using Disilane and Ozone or Water as Reactants. *J. Vac. Sci. Technol., A* **2023**, *41*, 042404.

(7) Collings, M. A.; Junige, M.; Cavanagh, A. S.; Wang, V. C.; Kummel, A. C.; George, S. M. Electron-Enhanced Atomic Layer Deposition of Ru Thin Films Using $Ru(DMBD)(CO)_3$ and Effect of Forming Gas Anneal. *J. Vac. Sci. Technol., A* **2023**, *41*, 062408.

(8) Ramsier, R. D.; Yates, J. T. Electron-Stimulated Desorption - Principles and Applications. *Surf. Sci. Rep.* **1991**, *12*, 246−378.

(9) Nishizawa, J.; Aoki, K.; Suzuki, S.; Kikuchi, K. Silicon Molecular Layer Epitaxy. *J. Electrochem. Soc.* **1990**, *137*, 1898−1904.

(10) Imai, S.; Iizuka, T.; Sugiura, O.; Matsumura, M. Atomic Layer Epitaxy of Si Using Atomic H. *Thin Solid Films* **1993**, *225*, 168−172.

(11) Utke, I.; Hoffmann, P.; Melngailis, J. Gas-Assisted Focused Electron Beam and Ion Beam Processing and Fabrication. *J. Vac. Sci. Technol. B* **2008**, *26*, 1197−1276.

(12) Thorman, R. M.; Kumar T P, R.; Fairbrother, D. H.; Ingólfsson, O. The Role of Low-Energy Electrons in Focused Electron Beam Induced Deposition: Four Case Studies of Representative Precursors. *Beilstein J. Nanotechnol.* **2015**, *6*, 1904−1926.

(13) Botman, A.; Mulders, J. J. L.; Hagen, C. W. Creating Pure Nanostructures from Electron-Beam-Induced Deposition Using Purification Techniques: A Technology Perspective. *Nanotechnol* **2009**, *20*, 372001.

(14) Mulders, J. J. L.; Belova, L. M.; Riazanova, A. Electron Beam Induced Deposition at Elevated Temperatures: Compositional Changes and Purity Improvement. *Nanotechnol* **2011**, *22*, 055302.

(15) Spencer, J. A.; Rosenberg, S. G.; Barclay, M.; Wu, Y. C.; McElwee-White, L.; Howard Fairbrother, D. Understanding the Electron-Stimulated Surface Reactions of Organometallic Complexes to Enable Design of Precursors for Electron Beam-Induced Deposition. *Appl. Phys. A: Mater. Sci. Process.* **2014**, *117*, 1631−1644.

(16) Thorman, R. M.; Kumar T P, R.; Fairbrother, D. H.; Ingólfsson, O. The Role of Low-Energy Electrons in Focused Electron Beam Induced Deposition: Four Case Studies of Representative Precursors. *Beilstein J. Nanotechnol.* **2015**, *6*, 1904−1926.

(17) Rohdenburg, M.; Boeckers, H.; Brewer, C. R.; McElwee-White, L.; Swiderek, P. Efficient NH_3-Based Process to Remove Chlorine from Electron Beam Deposited Ruthenium Produced from $(h^3\text{-}C_3H_5)Ru(CO)_3Cl$. *Sci. Rep.* **2020**, *10*, 10901.

(18) Rohdenburg, M.; Winkler, R.; Kuhness, D.; Plank, H.; Swiderek, P. Water-Assisted Process for Purification of Ruthenium Nanomaterial Fabricated by Electron Beam Induced Deposition. *ACS Appl. Nano Mater.* **2020**, *3*, 8352−8364.

(19) Spencer, J. A.; Barclay, M.; Gallagher, M. J.; Winkler, R.; Unlu, I.; Wu, Y. C.; Plank, H.; McElwee-White, L.; Fairbrother, D. H. Comparing Postdeposition Reactions of Electrons and Radicals with Pt Nanostructures Created by Focused Electron Beam Induced Deposition. *Beilstein J. Nanotechnol.* **2017**, *8*, 2410−2424.

(20) Perentes, A.; Hoffmann, P. Focused Electron Beam Induced Deposition of Si-based Materials from SiO_xC_y to Stoichiometric SiO_2: Chemical Compositions, Chemical-Etch Rates, and Deep Ultraviolet Optical Transmissions. *Chem. Vap. Deposition* **2007**, *13*, 176−184.

(21) Shawrav, M. M.; Taus, P.; Wanzenboeck, H. D.; Schinnerl, M.; Stöger-Pollach, M.; Schwarz, S.; Steiger-Thirsfeld, A.; Bertagnolli, E. Highly Conductive and Pure Gold Nanostructures Grown by Electron Beam Induced Deposition. *Sci. Rep.* **2016**, *6*, 34003.

(22) Wanzenboeck, H. D.; Fischer, M.; Svagera, R.; Wernisch, J.; Bertagnolli, E. Custom Design of Optical-Grade Thin Films of Silicon Oxide by Direct-Write Electron-Beam-Induced Deposition. *J. Vac. Sci. Technol. B* **2006**, *24*, 2755.

(23) Sobell, Z. C.; George, S. M. Electron-Enhanced Atomic Layer Deposition of Titanium Nitride Films Using an Ammonia Reactive Background Gas. *Chem. Mater.* **2022**, *34*, 9624−9633.

(24) Drinkwine, M. J.; Lichtman, D. Electron Stimulated Desorption: A Critical Review. *Prog. Surf. Sci.* **1977**, *8*, 123−142.

(25) Diebold, U. The Surface Science of Titanium Dioxide. *Surf. Sci. Rep.* **2003**, *48*, 53−229.

(26) Kim, S. K.; Hoffmann-Eifert, S.; Reiners, M.; Waser, R. Relation Between Enhancement in Growth and Thickness-Dependent Crystallization in ALD TiO_2 Thin Films. *J. Electrochem. Soc.* **2011**, *158*, D6−D9.

(27) Xie, Q.; Musschoot, J.; Deduytsche, D.; Van Meirhaeghe, R. L.; Detavernier, C.; Van den Berghe, S.; Jiang, Y. L.; Ru, G. P.; Li, B. Z.; Qu, X. P. Growth Kinetics and Crystallization Behavior of TiO_2 Films Prepared by Plasma Enhanced Atomic Layer Deposition. *J. Electrochem. Soc.* **2008**, *155*, H688−H692.

(28) Tan, L.-L.; Ong, W.-J.; Chai, S.-P.; Mohamed, A. R. Band Gap Engineered, Oxygen-Rich TiO_2 for Visible Light Induced Photocatalytic Reduction of CO_2. *Chem. Commun.* **2014**, *50*, 6923−6926.

(29) Weirich, T. E.; Winterer, M.; Seifried, S.; Hahn, H.; Fuess, H. Rietveld Analysis of Electron Powder Diffraction Data from Nanocrystalline Anatase, TiO_2. *Ultramicroscopy* **2000**, *81*, 263−270.

(30) Etacheri, V.; Seery, M. K.; Hinder, S. J.; Pillai, S. C. Oxygen Rich Titania: A Dopant Free, High Temperature Stable, and Visible-Light Active Anatase Photocatalyst. *Adv. Funct. Mater.* **2011**, *21*, 3744−3752.

(31) Gritsenko, V. A. Electronic Structure of Silicon Nitride. *Phys.-Usp.* **2012**, *55*, 498−507.

(32) Herzinger, C. M.; Johs, B.; McGahan, W. A.; Woollam, J. A.; Paulson, W. Ellipsometric Determination of Optical Constants for Silicon and Thermally Grown Silicon Dioxide via a Multi-Sample, Multi-Wavelength, Multi-Angle Investigation. *J. Appl. Phys.* **1998**, *83*, 3323−3336.
(33) Dong, D.; Irene, E. A.; Young, D. R. Preparation and Some Properties of Chemically Vapor-Deposited Si-Rich SiO_2 and Si_3N_4 Films. *J. Electrochem. Soc.* **1978**, *125*, 819−823.
(34) She, X.; Huang, A. Q.; Lucía, O.; Ozpineci, B. Review of Silicon Carbide Power Devices and Their Applications. *IEEE Trans. Ind. Electron.* **2017**, *64*, 8193−8205.
(35) Huang, J. J.; Militzer, C.; Wijayawardhana, C.; Forsberg, U.; Pedersen, H. Conformal and Superconformal Chemical Vapor Deposition of Silicon Carbide Coatings. *J. Vac. Sci. Technol., A* **2022**, *40*, 053402.
(36) Nishino, S.; Suhara, H.; Ono, H.; Matsunami, H. Epitaxial Growth and Electric Characteristics of Cubic SiC on Silicon. *J. Appl. Phys.* **1987**, *61*, 4889−4893.
(37) Sone, H.; Kaneko, T.; Miyakawa, N. In Situ Measurements and Growth Kinetics of Silicon Carbide Chemical Vapor Deposition from Methyltrichlorosilane. *J. Cryst. Growth* **2000**, *219*, 245−252.
(38) Linke, J.; Rinder, J.; Hahn, G.; Terheiden, B. Correlation Between the Optical Bandgap and the Monohydride Bond Density of Hydrogenated Amorphous Silicon. *J. Non-Cryst. Solids:X* **2020**, *5*, 100044.
(39) Gillis, H. P.; Choutov, D. A.; Steiner, P. A.; Piper, J. D.; Crouch, J. H.; Dove, P. M.; Martin, K. P. Low Energy Electron-Enhanced Etching of Si(100) in Hydrogen/Helium Direct-Current Plasma. *Appl. Phys. Lett.* **1995**, *66*, 2475−2477.
(40) Abrefah, J.; Olander, D. R. Reaction of Atomic Hydrogen with Crystalline Silicon. *Surf. Sci.* **1989**, *209*, 291−313.
(41) Krisyuk, V. V.; Koretskaya, T. P.; Turgambaeva, A. E.; Trubin, S. V.; Korolkov, I. V.; Debieu, O.; Duguet, T.; Igumenov, I. K.; Vahlas, C. Thermal Decomposition of Tungsten Hexacarbonyl: CVD of W-Containing Films Under Pd Codeposition and VUV Assistance. *Phys. Status Solidi C* **2015**, *12*, 1047−1052.
(42) Wnorowski, K.; Stano, M.; Matias, C.; Denifl, S.; Barszczewska, W.; Matejcík, S. Low-Energy Electron Interactions with Tungsten Hexacarbonyl - $W(CO)_6$. *Rapid Commun. Mass Spectrom.* **2012**, *26*, 2093−2098.
(43) Hones, P.; Martin, N.; Regula, M.; L vy, F. Structural and Mechanical Properties of Chromium Nitride, Molybdenum Nitride, and Tungsten Nitride Thin Films. *J. Phys. D: Appl. Phys.* **2003**, *36*, 1023−1029.
(44) Rosenberg, S. G.; Barclay, M.; Fairbrother, D. H. Electron Induced Reactions of Surface Adsorbed Tungsten Hexacarbonyl ($W(CO)_6$). *Phys. Chem. Chem. Phys.* **2013**, *15*, 4002−4015.
(45) Kim, S. H.; Kim, J. K.; Kwak, N.; Sohn, H.; Kim, J.; Jung, S. H.; Hong, M. R.; Lee, S. H.; Collins, J. Atomic Layer Deposition of Low-Resistivity and High-Density Tungsten Nitride Thin Films Using B_2H_6, WF_6, and NH_3. *Electrochem. Solid-State Lett.* **2006**, *9*, C54−C57.
(46) Klaus, J. W.; Ferro, S. J.; George, S. M. Atomic Layer Deposition of Tungsten Nitride Films Using Sequential Surface Reactions. *J. Electrochem. Soc.* **2000**, *147*, 1175−1181.
(47) Kelsey, J. E.; Goldberg, C.; Nuesca, G.; Peterson, G.; Kaloyeros, A. E.; Arkles, B. Low Temperature Metal-Organic Chemical Vapor Deposition of Tungsten Nitride as Diffusion Barrier for Copper Metallization. *J. Vac. Sci. Technol. B* **1999**, *17*, 1101−1104.
(48) Lee, B. H.; Yong, K. MOCVD of Tungsten Nitride Films Using $W(CO)_6$ and NH_3 for Cu Diffusion Barrier. *J. Electrochem. Soc.* **2004**, *151*, C594.
(49) Zheng, H. D.; Ou, J. Z.; Strano, M. S.; Kaner, R. B.; Mitchell, A.; Kalantar-Zadeh, K. Nanostructured Tungsten Oxide - Properties, Synthesis, and Applications. *Adv. Funct. Mater.* **2011**, *21*, 2175−2196.
(50) Locherer, K. R.; Swainson, I. P.; Salje, E. K. H. Transition to a New Tetragonal Phase of WO_3: Crystal Structure and Distortion Parameters. *J. Phys.: Condens. Matter* **1999**, *11*, 4143−4156.
(51) Subrahmanyam, A.; Karuppasamy, A. Optical and Electrochromic Properties of Oxygen Sputtered Tungsten Oxide (WO_3) Thin Films. *Sol. Energy Mater. Sol. Cells* **2007**, *91*, 266−274.
(52) Wong, H. Y.; Ong, C. W.; Kwok, R. W. M.; Wong, K. W.; Wong, S. P.; Cheung, W. Y. Effects of Ion Beam Bombardment on Electrochromic Tungsten Oxide Films Studied by X-Ray Photoelectron Spectroscopy and Rutherford Back-Scattering. *Thin Solid Films* **2000**, *376*, 131−139.
(53) Ikenoue, T.; Yoshida, T.; Miyake, M.; Kasada, R.; Hirato, T. Fabrication and Mechanical Properties of Tungsten Carbide Thin Films via Mist Chemical Vapor Deposition. *J. Alloys Compd.* **2020**, *829*, 154567.
(54) Pak, A.; Sivkov, A.; Shanenkov, I.; Rahmatullin, I.; Shatrova, K. Synthesis of Ultrafine Cubic Tungsten Carbide in a Discharge Plasma Jet. *Int. J. Refract. Met. Hard Mater.* **2015**, *48*, 51−55.
(55) Tanaka, S.; Bataev, I.; Oda, H.; Hokamoto, K. Synthesis of Metastable Cubic Tungsten Carbides by Electrical Explosion of Tungsten Wire in Liquid Paraffin. *Adv. Powder Technol.* **2018**, *29*, 2447−2455.
(56) Davey, W. P. The Lattice Parameter and Density of Pure Tungsten. *Phys. Rev.* **1925**, *26*, 736.
(57) Fuyuki, T.; Nakayama, M.; Yoshinobu, T.; Shiomi, H.; Matsunami, H. Atomic Layer Epitaxy of Cubic SiC by Gas Source MBE Using Surface Superstructure. *J. Cryst. Growth* **1989**, *95*, 461−463.
(58) Sumakeris, J. J.; Rowland, L. B.; Kern, R. S.; Tanaka, S.; Davis, R. F. Layer-by-Layer Growth of SiC at Low-Temperatures. *Thin Solid Films* **1993**, *225*, 219−224.
(59) Manzeli, S.; Ovchinnikov, D.; Pasquier, D.; Yazyev, O. V.; Kis, A. 2D Transition Metal Dichalcogenides. *Nat. Rev. Mater.* **2017**, *2*, 17033.
(60) Seravalli, L.; Bosi, M. A Review on Chemical Vapour Deposition of Two-Dimensional MoS_2 Flakes. *Materials* **2021**, *14*, 7590.
(61) Peterson, G. R.; Carr, R. E.; Marinero, E. E. Zirconium Carbide for Hypersonic Applications, Opportunities and Challenges. *Materials* **2023**, *16*, 6158.
(62) Shuo, W.; Kan, Z.; Tao, A.; Chaoquan, H.; Qingnan, M.; Yuanzhi, M.; Mao, W.; Weitao, Z. Structure, Mechanical and Tribological Properties of HfC_x Films Deposited By Reactive Magnetron Sputtering. *Appl. Surf. Sci.* **2015**, *327*, 68−76.
(63) Emig, G.; Schoch, G.; Wormer, O. Chemical Vapor Deposition of Hafnium Carbide and Hafnium Nitride. *J. Phys.* **1993**, *03*, C3-535.
(64) Wang, Y. G.; Liu, Q. M.; Liu, J. L.; Zhang, L. T.; Cheng, L. F. Deposition Mechanism for Chemical Vapor Deposition of Zirconium Carbide Coatings. *J. Am. Ceram. Soc.* **2008**, *91*, 1249−1252.
(65) Hong, J. N. F.; Mutalik, S.; Pescarmona, P. P.; Protesescu, L. Metal Borides: From Industrial Classics to Versatile Colloidal Nanocrystals for Energy, Catalysis, and Hard Coatings Applications. *Chem. Mater.* **2024**, *36*, 2147−2164.
(66) Al-Jothery, H. K. M.; Albarody, T. M. B.; Yusoff, P. S. M.; Abdullah, M. A.; Hussein, A. R. A Review of Ultra-High Temperature Materials for Thermal Protection System. *IOP Conf. Ser.:Mater. Sci. Eng.* **2020**, *863*, 012003.
(67) Opeka, M. M.; Talmy, I. G.; Zaykoski, J. A. Oxidation-Based Materials Selection for 2000°C Plus Hypersonic Aerosurfaces:: Theoretical Considerations and Historical Experience. *J. Mater. Sci.* **2004**, *39*, 5887−5904.
(68) Pierson, H. O.; Mullendore, A. W. The Chemical Vapor-Deposition of TiB_2 from Diborane. *Thin Solid Films* **1980**, *72*, 511−516.
(69) Pierson, H. O.; Mullendore, A. W. Thick Boride Coatings by Chemical Vapor-Deposition. *Thin Solid Films* **1982**, *95*, 99−104.
(70) Kim, H. Atomic Layer Deposition of Metal and Nitride Thin Films: Current Research Efforts and Applications for Semiconductor Device Processing. *J. Vac. Sci. Technol. B* **2003**, *21*, 2231−2261.
(71) Nicolet, M. A. Ternary Amorphous Metallic Thin-Films as Diffusion-Barriers for Cu Metallization. *Appl. Surf. Sci.* **1995**, *91*, 269−276.

https://doi.org/10.1021/acs.chemmater.5c00264
Chem. Mater. 2025, 37, 4652−4664